Redox Metal-Ligand Cooperativity Enables Robust and Efficient Water Oxidation Catalysis at Neutral pH with Macrocyclic Copper Complexes.

Pablo Garrido-Barros[1†], Dooshaye Moonshiram[2], Marcos Gil-Sepulcre[1], Primavera Pelosin[1], Carolina Gimbert-Suriñach[1], Jordi Benet-Buchholz[1] and Antoni Llobet[1,3*]

[1] Institute of Chemical Research of Catalonia (ICIQ), Barcelona Institute of Science and Technology (BIST), Tarragona, Spain, Avinguda. Països Catalans, 16,43007 Tarragona, Spain

[2] Instituto Madrileño de Estudios Avanzados en Nanociencia (IMDE A Nanociencia), Calle Faraday, 9, 28049 Madrid, Spain

[3] Departament de Química, Universitat Autònoma de Barcelona, 08193 Bellaterra, Spain

Reaction mechanism, water oxidation catalysis, water splitting, first row transition metal complexes, redox properties, redox non-innocent ligand

ABSTRACT: Water oxidation catalysis stands out as one of the most important reactions to design practical devices for artificial photosynthesis. The use of late 1st row transition metal (TM) complexes provides an excellent platform for the development of inexpensive catalysts with an exquisite control on their electronic and structural features via ligand design. However, the difficult access to their high oxidation states and the general labile character of their metal-ligand bonds pose important challenges. Herein, we explore a copper complex ($\mathbf{1}^{2-}$) featuring an extended, π-delocalized, tetraamidate macrocyclic ligand (TAML) as water oxidation catalysts, and compare its activity to analogous systems with lower π-delocalization ($\mathbf{2}^{2-}$ and $\mathbf{3}^{2-}$). Their characterization evidences a special metal-ligand cooperativity in accommodating the required oxidative equivalents using $\mathbf{1}^{2-}$ that is absent in $\mathbf{2}^{2-}$ and $\mathbf{3}^{2-}$. This consists in charge delocalization promoted by easy access to different electronic states at a narrow energy range, corresponding to either metal-centered or ligand-centered oxidations, which we identify as essential factor to stabilize the accumulated oxidative charges. This translates into a significant improvement in the catalytic performance of $\mathbf{1}^{2-}$ compared to $\mathbf{2}^{2-}$ and $\mathbf{3}^{2-}$, and leads to one of the most active and robust molecular complexes for water oxidation at neutral pH, with a k_{obs} of 140 s^{-1} at an overpotential of only 200 mV. In contrast, $\mathbf{2}^{2-}$ degrades under oxidative conditions, what we associate to impossibility of efficiently stabilize several oxidative equivalents via charge delocalization, resulting in highly reactive oxidized ligand. Finally, the acyclic structure of $\mathbf{3}^{2-}$ prevent its use at neutral pH due to acidic demetallation, highlighting the importance of the macrocyclic stabilization.

1. Introduction

The need to replace fossil fuels by a renewable and clean source of energy is increasingly urgent as the consequences of the global warming become more significant and irreversible.[1,2] Nowadays, besides the scientific community that has been actively working to come up with a solution during the last decades, policy makers and society in general are starting to mobilize in search for clean and sustainable energy vectors.[3,4,5] Artificial photosynthesis to produce solar fuels from water and sunlight is nowadays one of the most promising short-term strategies.[6,7,8,9,10] A common step in all the proposed photosynthetic schemes, both natural or artificial, is the catalytic oxidation of water to molecular oxygen (equation 1) in order to produce electrons and protons for the further reduction of protons to hydrogen (equation 2) or the reduction of other interesting substrates such as CO_2.[11,12,13,14] This oxidative half reaction has attracted the attention of researchers over years since overcoming its high kinetic barriers would largely solve the efficiency problems for a practical application.[15,16,17]

$$2H_2O \rightarrow O_2 + 4H^+ + 4e^-, E^0 = 1.23\,V\ vs.NHE\ at\ pH\ 0 \quad (1)$$

$$2H^+ + 2e^- \rightarrow H_2, E^0 = 0.0\,V\ vs.NHE\ at\ pH\ 0 \quad (2)$$

Molecular complexes offer a great platform to drive this reaction catalytically as their electronic and structural properties can relatively easily be fine-tuned by ligand modification in order to improve the catalytic efficiencies.[18, 19] Ultimately, molecular catalysts can be incorporated on electrodes and photoelectrodes leading to active molecular heterogeneous catalysts with an exquisite control in their properties.[20,21,22,2] However, the design of improved molecular catalysts relies on our understanding of the mechanistic pathways for water oxidation and the structure-activity relationships.[18] Although significant advances have been achieved in Ruthenium catalysts,[24] the knowledge regarding 1st row transition metals (TM) is still scarce and detailed understanding at a molecular level is generally lacking.[25,26] Therefore the rationalization of their design rules is indispensable in order to take advantage of their favorable properties including high abundance and non-toxicity.

Two important challenges for 1st row TM complexes are the ligand substitution lability and the accessibility to multiple oxidation states at relatively low potentials, and those are the main factors responsible for the catalyst degradation pathways (Figure 1a). Moreover, the requirement of using water as substrate and ideally as solvent poses the ligand protonation and subsequent metal decoordination as a competing process. Those phenomena are in sharp contrast with Ru complexes that are generally substitutionally inert and have access to high oxidation states within a narrow potential range via proton coupled electron transfer.

On the other hand, for abundant 1st row TM in general, the generation of high oxidation states resulting in active metal-oxo (M—O)[27] units is limited by the large potentials separating the different redox couples, which could favor alternative ligand oxidative degradation and/or metal oxide formation (Figure 1a). In particular Cu complexes at oxidation state (III) can only be obtained with strongly electron-donating ligands.[28,29,30,] Thus, to further facilitate access to formally high oxidation states, we[31] and others[32,33,34,35,36] have described the use of redox active ligands that are oxidized in a reversible manner. The storage of oxidative equivalents (holes) by both the metal center and the ligand helps the four-electron removal needed for the water oxidation reaction and thus widens the scope of useful molecular water oxidation catalysts (WOCs).[20]

Today the use of well-defined and rugged Cu WOCs is still limited to basic pH,[31,32,37,38,39,40,41,42] with very few examples reported at neutral pH featuring high overpotentials, slow kinetics and/or limited information about the long-term stability. [43,44,45] Further, a detailed analysis at a molecular level is frequently lacking, which is important to understand structure-activity relationships and the possible formation of copper oxides materials as the active catalytic species.[46,47,48,49]

In order to address the low acidic and oxidative stabilities without compromising the overpotential and catalytic rates, we focused our attention on the use of tetraamide macrocyclic ligands (TAML). Macrocyclic ligands are expected to provide additional stability to the Cu center with regard to related acyclic ligands such as H_4L3[31] (N1,N1'-(1,2-phenylene)bis(N2-methyloxalamide)) depicted in Figure 1b, via the "macrocyclic effect".[50,51,52,53,54,55] This should enhance the pH range of stability of the catalysts at the desired lower pH values. While those ligands also help to stabilize high oxidation states in the metal centers,[56] we consider their redox non-innocent character, which relies on the oxidation of the phenyl-bisamidate bridge similar to the corresponding acyclic analogues (see Figure 1c).[57]

While those units can accumulate up to two oxidative equivalents, the redox potentials for both oxidations are separated by more than 500 mV, evidencing the relatively difficult access to the second oxidation event and thus precluding their multiredox non-innocent character (accumulation of more than one oxidative equivalent). Moreover, although the redox non-innocence of these type ligands during water oxidation has been invoked, still high valent $M^{IV/V}$—O groups are required for initiating the catalytic process as experimentally evidenced, thus controlling the overall overpotential.[56,58,59,60,61,62,63]

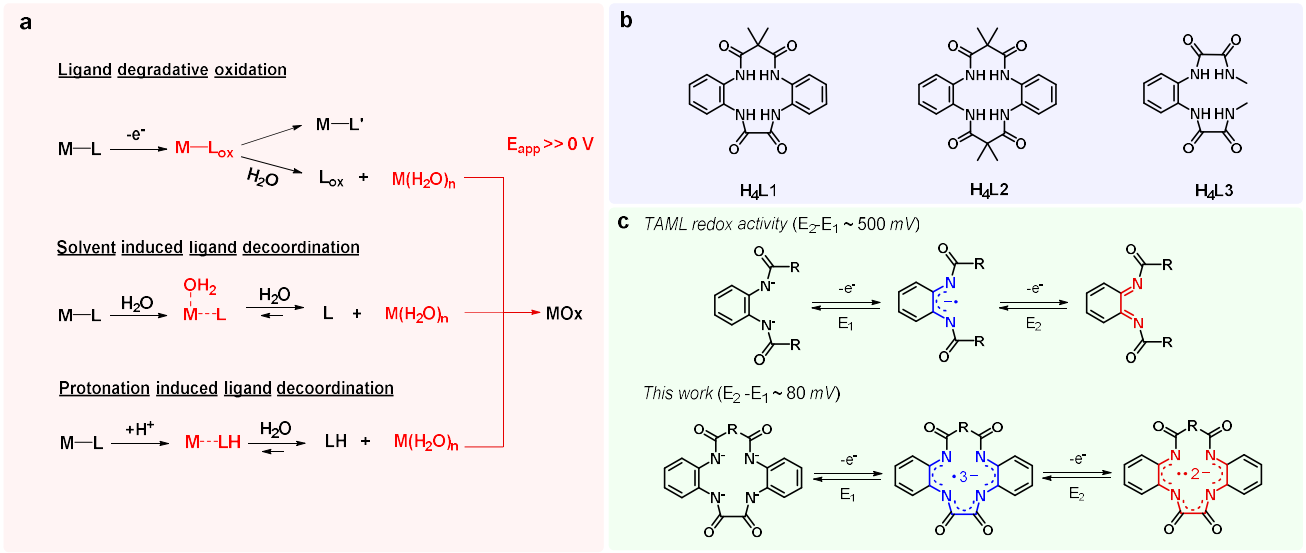

Figure 1. (a) Schematic representation of the main pathways for catalyst degradation under conditions used in water oxidation leading to the formation of metal-aquo complexes and free ligand. (b) Structure of the three tetraamidate ligands, including both macrocyclic and acyclic alternatives, discussed in this work. (c) Redox non-innocence TAML ligand *vs.* high π-delocalized $L1^{4-}$

We envision that the use of highly π-extended TAML with two phenyl-bisamidate units will allow access to several oxidations in the ligand at a lower potential range due to greater stabilization of the resulting radicals, rendering multi-redox active character (Figure 1c). Importantly, this will be key for accessing multiple oxidations with late transition metals such as copper given the limited access to their higher oxidation sates. We have focused our attention on the macrocyclic ligands depicted in Figure 1b, H_4L1 (15,15-dimethyl-8,13-dihydro-5H-dibenzo[b,h][1,4,7,10]tetraazacyclotridecine-6,7,14,16(15H,17H)-tetraone)[64] and H_4L2 (7,7,16,16-tetramethyl-5,9,14,18-tetrahydrodibenzo[b,i][1,4,8,11]tetraazacyclotetradecine-6,8,15,17(7H,16H)-tetraone)[65]. We anticipate that the use of such ligands with copper will also foster a larger metal-ligand electronic interaction, due to the usually higher covalency promoted by the more electronegative late transition metals. In this context, we report the synthesis, spectroscopic and electrochemical characterization of two new Cu complexes $[Cu^{II}L1]^{2-}$, $\mathbf{1}^{2-}$ and $[Cu^{II}L2]^{2-}$, $\mathbf{2}^{2-}$, together with their performance as catalysts for the water oxidation reaction. We compare those new complexes with previously reported acyclic analogue $\mathbf{3}^{2-}$.[31]

2. Results

2.1. Synthesis, structural and electronic properties of Cu(II) amidate complexes

The synthesis of the macrocyclic ligands H_4L1 and H_4L2 is reported in the Supporting Information, together with the corresponding characterization (Figures S1-S7). The synthesis of the Cu(II) complexes is straightforward and consists in mixing methanolic solutions of the deprotonated macrocyclic ligand and $Cu(ClO_4)_2$ as a metal precursor leading to the corresponding complexes in relatively good yields. The anionic Cu(II) complexes $\mathbf{1}^{2-}$ and $\mathbf{2}^{2-}$ obtained in this manner were characterized by elemental analysis, spectroscopic and electrochemical techniques and X-ray diffraction analysis.

Figure 2 shows the side views of the ORTEP plot for the anionic complexes $\mathbf{1}^{2-}$ and $\mathbf{2}^{2-}$ (top views in Figure S8). Both feature a square-planar coordination environment similar to the analogous acyclic complex $[Cu^{II}L3]^{2-}$, $\mathbf{3}^{2-}$, and its family of related substituted complexes.[31] The strong σ-donor character of the amidate groups compensates for the electron deficient configuration of the 17 e⁻ complexes and ensures strong metal-ligand bonds reflected in the short Cu-N distances and high stabilization of the d^9 Cu(II) ion as a square planar four-coordinated metal center. In the case of complex $\mathbf{1}^{2-}$ bearing the 13-membered ring ligand $L1^{4-}$, those distances are in the range of 1.895(7)-1.928(8) Å, significantly shorter than those formed by the 14-membered ring ligand in $\mathbf{2}^{2-}$ (1.922(6)-1.941(6) Å), due to the larger size and rigidity of the macrocyclic ligand $L2^{4-}$. In both cases, the metal-ligand distances are shorter than the ones found for the family of analogous Cu(II) complexes bearing the acyclic tetraamidate ligand $L3^{4-}$ (1.938-1.953 Å),[66] evidencing the stronger Cu-N bond interactions in the case of the macrocyclic complexes.

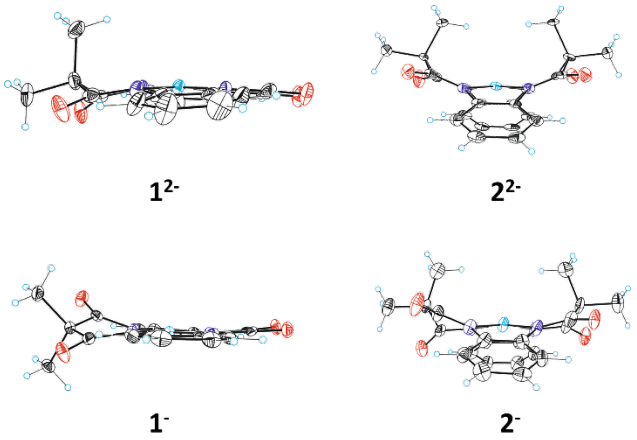

Figure 2. ORTEP drawing (thermal ellipsoids drawn at a 50 % probability level) showing side views of the cationic structure of **1**²⁻, **1**⁻, **2**²⁻, and **2**⁻. Colour code: C, black; N, blue; O, red; Cu, light blue.

The short Cu-N bond lengths obtained for the macrocyclic complexes **1**²⁻ and **2**²⁻ together with the lower basicity of the phenyl-bisamidate ligands than alkyl amidates, is reflected in their relative stability in aqueous solutions as compared to the acyclic **3**²⁻. While the latter decoordinates at pH lower than 10, the former are stable all the way down to pH 7 (Figures S13-S15) which is highly desirable for their potential application as molecular electroanodes.[67,68]

X-ray absorption near edge and extended X-ray absorption fine structure spectroscopies (XANES and EXAFS respectively) were further used to characterize the electronic and structural properties of complex **1**²⁻ and the results are shown in Figure 3 and Figure S9. The EXAFS simulation carried out for **1**²⁻ shows a remarkable agreement between the simulated Cu-N bonding distances and those obtained by X-ray diffraction (XRD) (Table S1). In addition, the XANES spectra of **1**²⁻ further shows a noticeable pre-edge feature at low photon energies, 8979.0 eV, corresponding to the 1s → 3 d electronic transition[69,70,71] as well as a main peak along the rising edge region at ~8987 eV commonly observed in Cu(II) square planar complexes (Figure 3a).[72,20] This transition is assigned to a metal localized 1s → 4p transition with "shakedown" contribution arising from a coupled ligand to metal charge transfer (LMCT) transition.[73]

The extended π-delocalization over the two phenyl groups and the oxamide bridge in ligand L1⁴⁻ is responsible for the nearly flat geometry of complex **1**²⁻ in contrast to complex **2**²⁻, where the presence of two dimethylmalonamide bridges with sp³ quaternary carbons breaks the π-conjugation between both phenyl groups. This results in a distorted structure where the two phenyl groups lay below the plane formed by the four N atoms bonded to the Cu center (the angle formed by the two phenyl rings is 50.1°) as can be observed in Figure S8 for **2**²⁻.

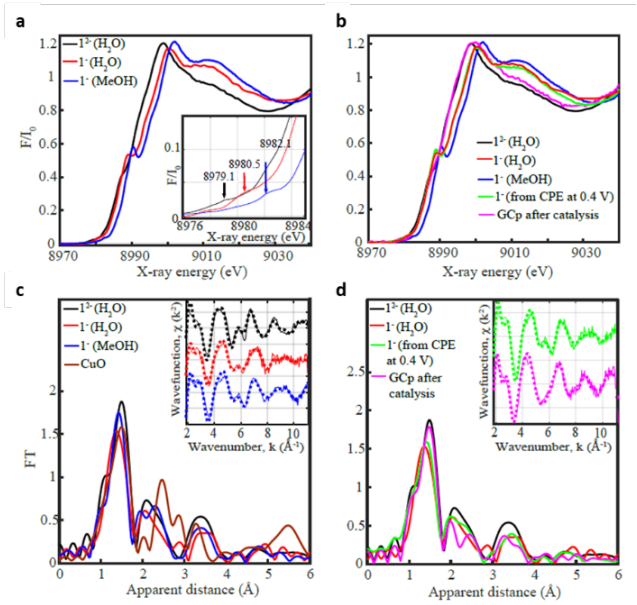

Figure 3. (a) Normalized Cu K-edge XANES of complex **1**²⁻ (1 mM) in water (black trace) and its oxidized analogous **1**⁻ (1 mM) in water (red trace) and methanol (blue trace) prepared by chemical oxidation with I_2. Inset. Zoom in of the pre-edge regions. (b), same as in (a) for 1 mM **1**²⁻ (black trace), chemically synthesized **1**⁻ (red and blue trace), electrochemically synthesized **1**⁻ (green trace), and a GC plate electrode used for a CPE (magenta trace) of a 1 mM **1**²⁻ at pH 7 with E_{app} = 1.25 V. (c) Experimental Fourier transforms of k²-weighted EXAFS spectra for complex **1**²⁻ (1 mM) in water (black trace), chemically synthesized **1**⁻ (1 mM) in water (red trace) and methanol (blue trace), and solid CuOx (shown in brown). Inset. Corresponding Back Fourier transforms. (d) same as in (c) for 1 mM **1**²⁻ (black trace), its chemically oxidized analogous **1**⁻ (red trace), electrochemically synthesized **1**⁻ (green trace) and a GC plate electrode after CPE of a 1 mM **1**²⁻ at pH 7 with E_{app} = 1.25 V (magenta trace). Inset. Back Fourier transformed experimental (solid lines) and fitted (dashed lines) k²[χ(k)]. See the SI for additional experimental details.

The delocalization phenomenon is also manifested in the UV-vis spectra of **1**²⁻ and **2**²⁻ in organic solvents and in water, where complex **1**²⁻ presents two new bands at 390 and 550 nm that can be tentatively assigned to low energy ligand-to-metal or ligand-to-ligand charge transfer as a consequence of the smaller difference in the energy levels (Figures S10-S12).[74] In contrast, these transitions occur at significantly higher energy (280-310 nm) in the case of **2**²⁻ due to the lower delocalization. Time dependent Density Functional Theory (TD-DFT) simulations of the UV-vis spectra performed on complexes **1**²⁻ and **2**²⁻ fully supports these assignments (Figures S66-S69). Similarly, in the case of **3**²⁻, those transitions also feature higher energy (500 and 340 nm) than in **1**²⁻, but lower than **2**²⁻ probably due to higher electronic delocalization through the (bis)amidate bridges compared to the dimethylmalonamide bridges in complex **2**²⁻.

2.2 High oxidation states of Cu amidate complexes in organic solvents

The one electron oxidized Cu(III) species, **1**⁻ and **2**⁻, can be obtained electrochemically or chemically using iodine as oxidant (see Supporting Information for de-

tailed synthesis). Crystal structures of both complexes were obtained and their ORTEP views are presented in Figure 2 and Figure S8. It can be appreciated that the Cu centers have the typical square planar D_{4h} type of geometry expected for d^8 ions. In the case of $\mathbf{1}^-$, the Cu-N distances are in average around 0.18 Å reduced as compared with its Cu(II) homologue which reflects the relative flexibility of the ligand adopting a more constrained conformation at oxidation state III. Similar results can be extracted from the X-ray structure of $\mathbf{2}^-$ whose ORTEP drawing is also shown in Figure 2. The Cu-N distances extracted from the simulation of EXAFS spectra of $\mathbf{1}^-$ in solid state are also in very good agreement with the contraction observed in the X-ray data (Figure S9 and Table S1). In addition, the XANES spectrum shows a pre-edge at 8982.1 eV for the Cu(III) complex $\mathbf{1}^-$ that is 3.0 eV higher than the Cu(II) $\mathbf{1}^{2-}$, in agreement with related complexes previously described in the literature .[20,76,77,78]

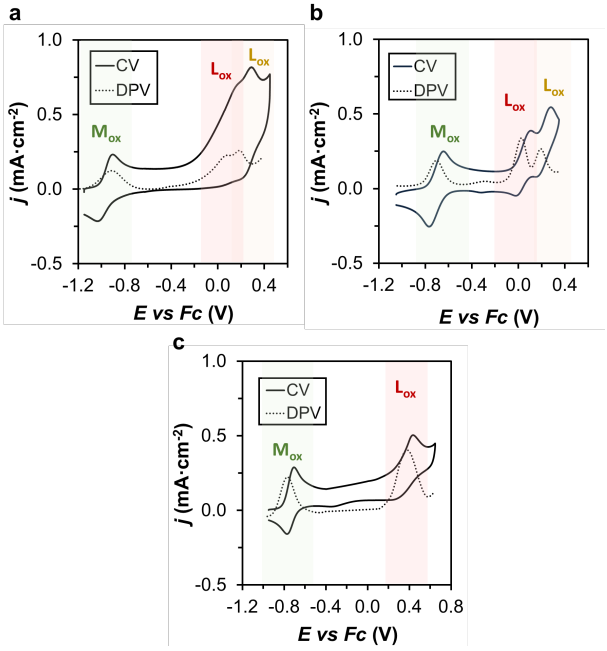

Figure 4. (a) CV and DPV of a 1 mM MeCN solution of (a) $\mathbf{1}^{2-}$ (b) $\mathbf{2}^{2-}$ and (c) $\mathbf{3}^{2-}$, using 0.1 M $TBAPF_6$ as supporting electrolyte and a glassy carbon as a working electrode.

The redox properties of these Cu complexes were investigated by means of cyclic voltammetry (CV) and differential pulse voltammetry (DPV) techniques in MeCN. A CV and DPV of $\mathbf{1}^{2-}$, $\mathbf{2}^{2-}$ and $\mathbf{3}^{2-}$ is presented in Figure 4 and Figure S16. The CV show a chemically reversible wave associated with Cu(III)/Cu(II) redox couple at $E_{1/2}$ = -0.90 V and -0.70 V *vs*. Ferrocene (Fc) for macrocyclic complexes $\mathbf{1}^{2-}$ and $\mathbf{2}^{2-}$ respectively, and $E_{1/2}$ = -0.75 V for $\mathbf{3}^{2-}$ consistent with previous results.[31] Those low redox potentials evidence the high stability of the generated Cu(III) species due to the tetraanionic character of the ligand that forces a square-planar geometry typical from d8 Cu(III) complexes.[79] The 200 mV lower potential for $\mathbf{1}^{2-}$ is associated with the stronger bonds and shorter Cu-N distances as indicated in the previous section and reflect a strong sigma donation capacity due to the reduced sized of the 13-membered ring macrocycle as opposed to the 14-membered ring of $L2^{4-}$. In case of $\mathbf{3}^{2-}$, the more flexible ligand backbone might be responsible for a greater stabilization of the Cu(III) center as compared to complex $\mathbf{2}^{2-}$ leading to a slightly lower redox potential despite their close Cu-N distances in the Cu(II) state. DFT calculations of the first redox process for these complexes are in good agreement with the observed potentials and satisfactorily reproduce the mentioned difference between them (Figures S70 and S71 and Ref 31).

Interestingly, at higher anodic potentials the CV of $\mathbf{1}^{2-}$ and $\mathbf{2}^{2-}$ show the presence of two more redox processes that are associated with ligand based π-electron oxidations. Whereas for $\mathbf{2}^{2-}$ they are chemically reversible, for $\mathbf{1}^{2-}$ they appear as chemically quasi-reversible. The separation in both ligand-centered waves is around 80 and 180 mV for $\mathbf{1}^{2-}$ and $\mathbf{2}^{2-}$ respectively, which contrasts with the oxidation at TAML ligands containing only one phenyl-bisamidate group where both waves are separated by more than 500 mV.[57] This is also consistent with the CV of complex $\mathbf{3}^{2-}$, which features only one ligand-based oxidation in the same potential range (Figure 4c). These results put forward the easier access to higher oxidation states at the ligand when using $L1^{4-}$ and $L2^{4-}$ *vs*. $L3^{4-}$ or the previously reported TAML ligand. Further, the 80 mV difference between the two ligand based redox couples in $L1^{4-}$ might be explained due to high delocalization of the generated radical. Density Functional Theory (DFT) calculations in organic solvents of new macrocyclic complexes show the ligand-centered SOMO corresponding to ligand based oxidations (Figures S70 and S71). The different degree of π-delocalization is evidenced comparing the SOMO of oxidized complex **1** complex, which is extended to both phenyl-bisamidate units, with that of complex **2**, featuring less contribution of the second phenyl-bisamidate unit.

2.3 High oxidation states of Cu amidate complexes in aqueous solutions

Figure 5 shows the CV of complexes $\mathbf{1}^{2-}$, $\mathbf{2}^{2-}$ and $\mathbf{3}^{2-}$ at pH 12 and 7 (further CV and DPV in Figures S17 and S18). All the redox potential in aqueous solution are versus NHE. At both pH values, $\mathbf{1}^{2-}$ and $\mathbf{2}^{2-}$ show the presence of one electron wave followed by second catalytic wave at higher potentials, similar to what was found for complex $\mathbf{3}^{2-}$ at pH 12. To elucidate the nature of these redox transitions in aqueous solutions a series of spectroscopic experiments were carried out that are described below.

The structural properties of complex $\mathbf{1}^{2-}$ and its one electron oxidized species $\mathbf{1}^-$ (obtained by chemical oxidation, see SI) in aqueous solution were studied by X-ray absorption (XAS) spectroscopy, Nuclear Magnetic Resonance (NMR) and Electron Paramagnetic Resonance (EPR). Complex $\mathbf{1}^-$ was also prepared via controlled potential electrolysis (CPE) at 0.4 V vs NHE for comparative XAS study (see SI for further details). Surprisingly the XANES spectrum for $\mathbf{1}^-$ in pH 7 solution shows a pre-edge at 8990.5 eV that is just in between the expected value for Cu(II) and Cu(III) suggesting that in aqueous solution the first oxidation process is not entirely metal based in contrast with MeOH solution. This is in agreement with ^{1}H-NMR spectroscopy of $\mathbf{1}^-$, which in MeOH (Figure S27) displayed the typical diamagnetic behavior expected for a D_{4h} symmetry d^8 ion but in D_2O, it showed no resonances in the 0-10 ppm range in agreement with a paramagnetic behavior. These observations indicate a

ligand-centered oxidation in water solution, which is further supported by EPR spectroscopy of $\mathbf{1}^{-}$, which is silent in MeOH whereas in H_2O displays EPR signal, consistent with paramagnetic behavior derived from a ligand centered oxidation (Figure 5d and S29).

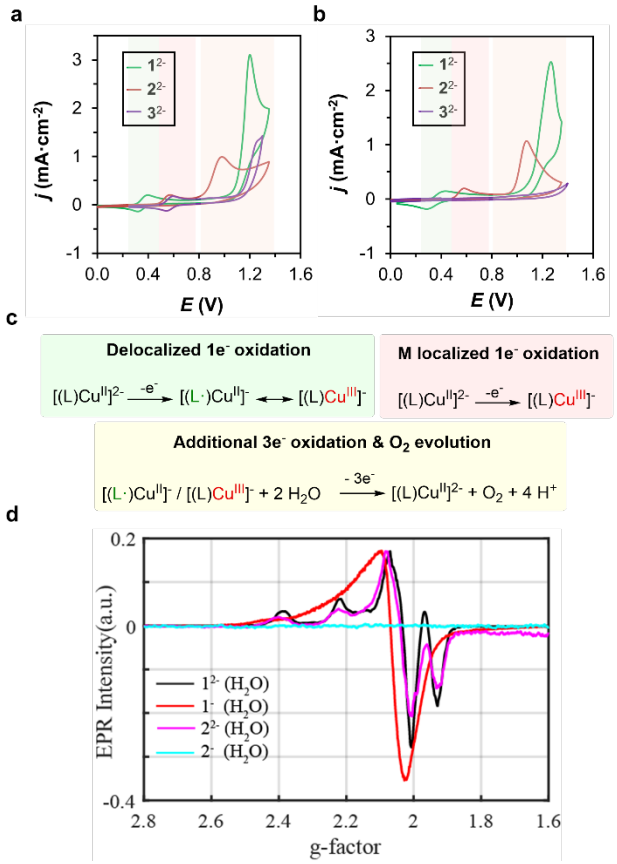

Figure 5. (a) CV of 1 mM $\mathbf{1}^{2-}$ (green trace), $\mathbf{2}^{2-}$ (red trace) and $\mathbf{3}^{2-}$ (purple trace) in aqueous solution using phosphate buffer at pH 12 with an ionic strength of 0.1 M. A BDD electrode was employed as a working electrode and the scan rate was set to 100 mV·s^{-1}. (b) CV of 1 mM $\mathbf{1}^{2-}$ (green trace), $\mathbf{2}^{2-}$ (red trace) and $\mathbf{3}^{2-}$ (purple trace) in aqueous solution using phosphate buffer at pH 7 with an ionic strength of 0.1 M. Similar experimental set up was used as in Figure 5a. (c) Schematic representation of the different oxidation events taking place in the CVs of complexes $\mathbf{1}^{2-}$-$\mathbf{3}^{2-}$. **(d)** X-band EPR spectra (20 K) $\mathbf{1}^{2-}$, $\mathbf{1}^{-}$, $\mathbf{2}^{2-}$ and $\mathbf{2}^{-}$, in H_2O (0.1 mM). **Color code:** Shading colors in Fig.5a and 5b of the redox events refers to the redox processes indicated in Fig. 5c.

Therefore, we described $\mathbf{1}^{-}$ in water as a triplet ground state (S=1) with ferromagnetic coupling between the S=1/2 d9 Cu(II) center and the S=1/2 radical ligand $(L1)^{3\cdot-}$. The low zero-field splitting (ZFS) allows for EPR transitions using standard X-band microwave source. This EPR characterization is supported by analogous square-planar, Cu(II) complexes bearing phenoxyl radical ligands previously reported.[□□,□1,□2] Alternative metal center oxidation or antiferromagnetic coupling of metal and ligand radicals is discarded since they would generate EPR-silent signals. The ferromagnetic behavior in $\mathbf{1}^{-}$ is explained by the absence of overlapping between the orbitals hosting the unpaired electrons, since the dx^2-y^2 of the metal center are orthogonal to the π-system of the ligand (Fig. S73).[83] The electronic delocalization in this triplet species is responsible for the broadening of the EPR signal and prevents hyperfine coupling resolution.[84,85,86] This contrast with the hyperfine splitting observed in the S=1/2 species $\mathbf{1}^{2-}$ with a localized unpaired electron in the metal center. In agreement with this, the EPR simulation of $\mathbf{1}^{2-}$ and $\mathbf{1}^{-}$ in H_2O show clearly different g-factors and hyperfine splitting (Figure 5) illustrating the different electronic environments. G values, g_{xx} of 2.138, g_{yy} of 2.045 and g_{zz} of 1.940, with A_{xx} of 215 G could be extracted from the EPR simulation of $\mathbf{1}^{2-}$ in H_2O (Figure S30) whereas the simulation of $\mathbf{1}^{-}$ assuming a triplet ground state yielded g_{xx}, g_{yy} and g_{zz} values of 2.230, 2.050 and 2.050 respectively, together with zero field splitting parameters of D and E to be 40 G and 5 G respectively (Figure S30). This description was further supported by DFT where it is found that the low energy triplet structure for $\mathbf{1}^{-}$ has a SOMO centered in the ligand with π-character and spin density entirely delocalized between the metal center and the π-system of $L1^{4-}$ (Figure S73). The alternative calculated singlet structure corresponding to metal oxidation centered in the d-orbitals has a similar energy with only 0.7 kcal·mol^{-1} difference. The spin crossover phenomenon clearly demonstrates the close proximity between the two different electronic states corresponding to accommodation of the oxidative equivalent in either metal d-orbitals or ligand π-delocalized orbitals respectively.

Furthermore, UV-vis analysis of the oxidized species by spectroelectrochemistry in aqueous solution shows a distinguishable decrease of the bands in the UV region (at around 300 nm) which is again consistent with the generation of partial radical character in the π-system of the ligand, weakening the π-π * transitions (Figures S36-S37).[20,87] The fact that the spin state, and thus the specific electronic structure of complex $\mathbf{1}^{-}$, is dependent on the solvation effects further evidences the existence of a large degree of degeneration in its frontier orbitals. This reflects a close energy match between the metal d orbitals and ligand π-system that is absent in previous Fe or Co TAML complexes.[56,57,58,59,60]

In sharp contrast, the ^{1}H-NMR spectrum for $\mathbf{2}^{-}$ in MeOH and D_2O are basically identical thus indicating that the first oxidation is metal based and that the spin crossover phenomena just described for $\mathbf{1}^{-}$ does not occur in $\mathbf{2}^{-}$ (Figure S28). In addition, $\mathbf{2}^{2-}$ in H_2O shows similar features to $\mathbf{1}^{2-}$, with G values, g_{xx} of 2.150, g_{yy} of 2.060 and g_{zz} of 1.940, with A_{xx} of 215 G (Figure S30) while complex $\mathbf{2}^{-}$ is EPR silent consistent with the assignment of a Cu(III) species. Those differences with $\mathbf{1}^{2-}$ reflects the importance of the relative energy of the molecular orbitals generated by π-delocalization.

2.4 Water Oxidation Catalysis by Cu amidate complexes

The CV in Figure 5 at pH 12 shows the presence of a second wave that is catalytic in nature at high anodic potentials. Complex $\mathbf{1}^{2-}$ has the largest catalytic wave with its foot situated at approx. 1.0 V which is about 100 mV lower than that of the acyclic complex $\mathbf{3}^{2-}$. For $\mathbf{2}^{-}$ the foot of the catalytic wave starts at approx. 0.8 V but the III/II waves disappear after catalysis, importantly indicating the disappearance of the initial molecular complex from the double layer. At pH 7, the acyclic complex decomposes and thus there is no electroactivity associated

with $\mathbf{3}^{2-}$, in sharp contrast with the stability displayed by $\mathbf{1}^{2-}$ and $\mathbf{2}^{2-}$. At pH 7, the foot of the catalytic wave for $\mathbf{1}^{2-}$ starts at approx. 1.0 V that represents an overpotential of *ca.* 200 mV whereas for $\mathbf{2}^{2-}$ the foot of the catalytic wave starts at approx. 0.9 V and represent an overpotential of only 100 mV. However, while for $\mathbf{1}^{2-}$ the III/II wave is fully reversible after catalysis, the reversibility is lost for $\mathbf{2}^{2-}$ indicating again the poor performance of the latter as a water oxidation catalyst.

These data manifests how small variations on ligand structure have an extraordinary impact in catalyst performance in terms of catalytic current, overpotential and stability. Here the right size and electronic structure of the 13-membered ring macrocycle satisfactorily fits the geometrical and electronic demands of both Cu(II) and Cu(III) and thus generates a very rugged catalyst. Enlarging the cavity by one more unit generating a 14-membered ring with reduced π-delocalization has a catastrophic effect on the stability of the catalyst.

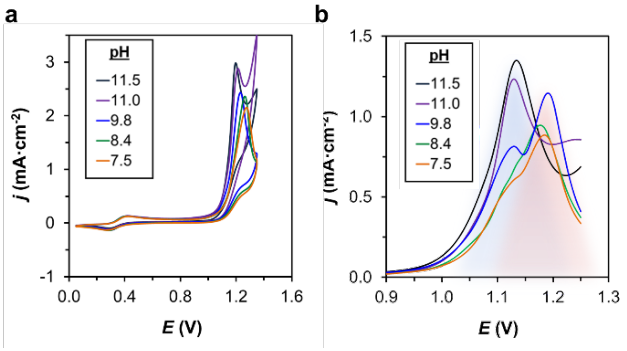

Figure 6. (a) CV of aqueous solutions at different pH containing 1 mM of complex $\mathbf{1}^{2-}$ in a 0.1 M phosphate buffer solution. A BDD electrode was employed as a working electrode and the scan rate was set to 100 mV·s^{-1}. (b) DPV of aqueous solutions at different pH containing 1 mM of complex $\mathbf{1}^{2-}$ in the same conditions as in **Figure 6a**.

The redox properties of $\mathbf{1}^{2-}$ and $\mathbf{2}^{2-}$ were further investigated as a function of pH by CV and DPV as shown in Figure 6 and Figures S32-S34. It is interesting to realize that at the 7-10 pH range there are two different catalytic processes for $\mathbf{1}^{2-}$ that can be easily identified in the DPV experiment, which implies an additional oxidation process. At the pH range 11-12, there is a single electrocatalytic process in the potential range studied. This suggests that at high pH (for instance at pH 11) after the removal of two electrons from the $\mathbf{1}^{2-}$ and a further hydroxido coordination, the new species **[1(OH)]**$^{-}$ generated is very active towards O-O bond formation and O_2 release, similar to previous observations with catalyst $\mathbf{3}^{2-}$. However, at pH 7, the kinetics of O-O bond formation will be slower because the [OH^{-}] is four orders of magnitude lower. Access to an additional electron removal generating the neutral species **[1(OH)]** will generate a much more electrophilic oxygen at the Cu-OH group that can also be responsible for the water oxidation catalysis at neutral pH. These reaction pathways are supported by DFT calculations (*vide infra*).

Spectroelectrochemistry performed in an optically transparent thin layer electrochemical (OTTLE) cell reveals the UV-vis spectra corresponding to the different redox process observed in the CV (Figures S36-S37). At redox potentials above 0.4 V the UV-vis spectrum for $\mathbf{1}^{-}$ is obtained showing small changes at the UV region with regard to that of $\mathbf{1}^{2-}$, consistent with the proposed ligand oxidation. Scanning to catalytic potentials and returning to the initial values, the UV-vis spectrum remains constant and is consistent with the high stability of the catalyst. Under catalytic potentials, similar features to those corresponding to $\mathbf{1}^{-}$ are obtained, with slightly lower absorbance in the UV region probably due to the further oxidation of the ligand in the resting state.

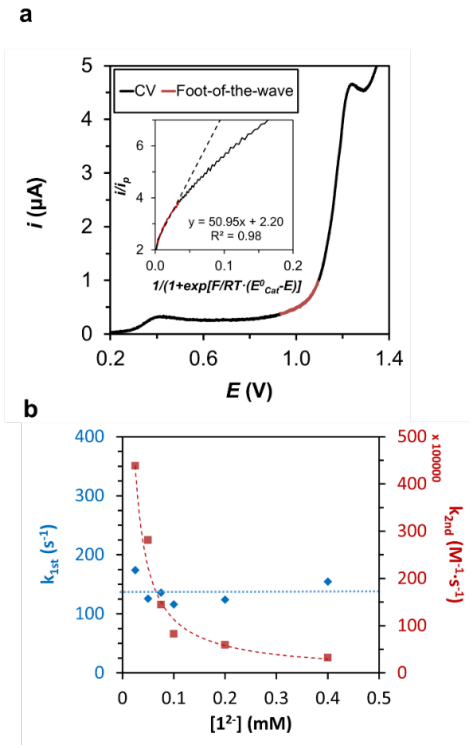

Figure 7. (a) Linear sweep voltammetry of an aqueous solution at pH 7 containing 1 mM of complex $\mathbf{1}^{2-}$ with 0.1 M phosphate buffer. BDD was employed as working electrode and at scan rate of 100 mV·s^{-1}. The red trace represents the data used for the foot-of-the-wave analysis (FOWA). The inset figure shows the FOWA under these conditions, where the red trace represent again the data used for the linear fit derived from FOWA equations. The black dashed line represents the ideal response of the system. (b) Plot of the observed kinetic constant calculated with FOWA assuming a first order mechanism (blue trace) or a second order mechanism (red trace) in catalyst.

To extract more information about this system a kinetic analysis was also carried out for $\mathbf{1}^{2-}$ based on foot of the wave analysis (FOWA).[90] It has been performed at pH 7 and 12 within the concentration range of 10-400 μM, and the results are reported in Figure 7 and Figure S35. A value of 200 s^{-1} for the k_{obs} (TOF_{max}) is obtained at pH 12 that is around two order of magnitude higher than that obtained for $\mathbf{3}^{2-}$. At pH 7, a k_{obs} of 140 s^{-1} is obtained that is among the highest reported for first row transition metals at pH 7 (*vide infra*).[26] Further, the plot of observed k_{obs} *vs.* catalyst concentration indicates a first order behavior with regard to $\mathbf{1}^{2-}$ and thus suggests that the O-O bond formation occurs via a water nucleophilic attack (WNA) pathway.[88]

2.5 DFT characterization of water oxidation

With all these data in hand, we additionally performed DFT calculations for complex $\mathbf{1}^{2-}$ (Figures S72-S78) in order to characterize the electronic states and coordination environments of the oxidized species responsible for catalytic activity. A summary of the results is shown in Figure 8 and Schemes S1 and S2.

As already discussed, in aqueous solution the first one electron oxidation leads to a triplet $\mathbf{1}^{-}$ species where the unpaired electrons are mainly delocalized all over the complex (Figure S73). Analysis of the SOMO clearly shows the oxidation being centered in the π-orbitals of the ligand with low contribution of d_{xz} and d_{yz} orbitals of the metal due to π-type interactions. This species is very close in energy to the singlet species corresponding to an oxidation centered in the metal d orbitals as discussed previously. This small energy difference could promote stabilization of the oxidative equivalents by easy access to both electronic structures giving rise to charge delocalization (Figure 8B, Figure S73). The coordination of a water or OH^- ligand to $\mathbf{1}^{-}$ is energetically unfavored. However, a second one electron removal to generate **1** yields a quartet species with SOMOs centered on the π-orbitals of the ligand (Figure S74). Once again, the alternative doublet species, where the second oxidation is mainly accommodated in the metal d orbitals, is very close in energy (2.1 kcal·mol^{-1}) suggesting high degeneration in the different electronic structures. The coordination of a hydroxido ligand is now favored by ΔG^{o} = -1.1 kcal·mol^{-1}, leading to $\mathbf{[1(OH)]}^{-}$ with a quartet multiplicity. This species has similar spin distribution and SOMOs as in **1**, with partial contribution of hydroxo-centered orbitals (see Figure S75). At pH 12, the $\mathbf{[1(OH)]}^{-}$ species is responsible for the O-O bond formation that leads to oxygen release and regenerates the initial Cu complex. This step has also been calculated and a mechanism based on single electron transfer-water nucleophilic attack (SET-WNA) was found operative for the O-O bond formation, in a similar manner as proposed recently for several copper complexes including $\mathbf{3}^{2-}$ (Scheme S2).[□□,31] In this mechanism, a first single electron transfer (SET) from an external hydroxide molecule leads to the formation of a 2 centers-3 electrons (2c-3e) intermediate where the ligand has been reduced by one electron (Figure S77). Further shortening of the O-O bond led to a second SET to form a hydroperoxo species with concomitant metal reduction to its initial oxidation state (Figure S78). Electron and proton removal from this species via proton coupled electron transfers (PCET) eventually results in the formation of oxygen and recovery of initial complex $\mathbf{2}^{2-}$.

However, at neutral pH, a third oxidation is observed under catalytic conditions that is consistent with an additional oxidized species. DFT proposes the formation of a triplet species **1(OH)** that would be responsible for the O-O bond formation at pH 7 (Figure S76). Here the one electron removal from the ligand leads to a spin density delocalized among the metal center, the OH^- ligand and one of the phenyl rings of the $L1^{4-}$ ligand. The LUMO and SOMO are thus centered on the ligand π-system, where two electrons alfa and one electron beta have been removed leading to only one unpaired electron in the ligand. In this case, calculation of the alternative electronic structure corresponding to a metal center oxidation and two unpaired electrons in the ligand remained elusive since in both cases the resulting electronic structure would also corresponds to a triplet states with small differences in energy. Instead, a singlet state could be optimized, also associated to a Cu(III) complex with no unpaired electrons in the ligand (alfa and beta electrons were removed corresponding to a closed-shell configuration). This singlet state is still close in energy (ΔG = 6.3 kcal·mol^{-1}) and potentially represents a higher limit for the energy of the alternative metal/ligand oxidized triplet species that we were not able to find. Once again, a SET-WNA mechanism could operate to promote O-O bond formation with the generation of the 2c-3e intermediate and further formation of a hydroperoxo species (Scheme S2 and Figures S77 and S78).

When the similar triply oxidized species is investigated for catalyst $\mathbf{2}^{2-}$ ($\mathbf{2}^{+}$, before OH^- coordination), a singlet species results as the most stable electronic structure where one oxidative equivalent is accumulated in the metal center and two in the ligand (corresponding to the removal of an alfa and a beta electron). In this species, the LUMO is mainly centered in one of the phenyl rings (Figure S79). Addition of a hydroxide ligand to the apical position of the metal center in $\mathbf{2}^{+}$ leads to the exothermic hydroxo attack to a carbon atom in the oxidized phenyl ring forming a C-O bond (Figure S80). This evidences the potential oxidative degradation pathways of this complex and is in good agreement with its poor performance as a water oxidation catalyst.

As previously reported via experiments and DFT,[31,89] catalyst $\mathbf{3}^{2-}$ performs water oxidation at basic pH via a first oxidation in the metal and a second oxidation in the ligand, which generates the active intermediate towards O-O bond formation. Here, the acyclic tetra-amidate ligand can only accommodate one oxidative equivalent in the studied potential range. This prevents further oxidation and generation of reactive species with an oxidized ligand as in complex $\mathbf{2}^{2-}$, which was identified as responsible for the oxidative degradation process.

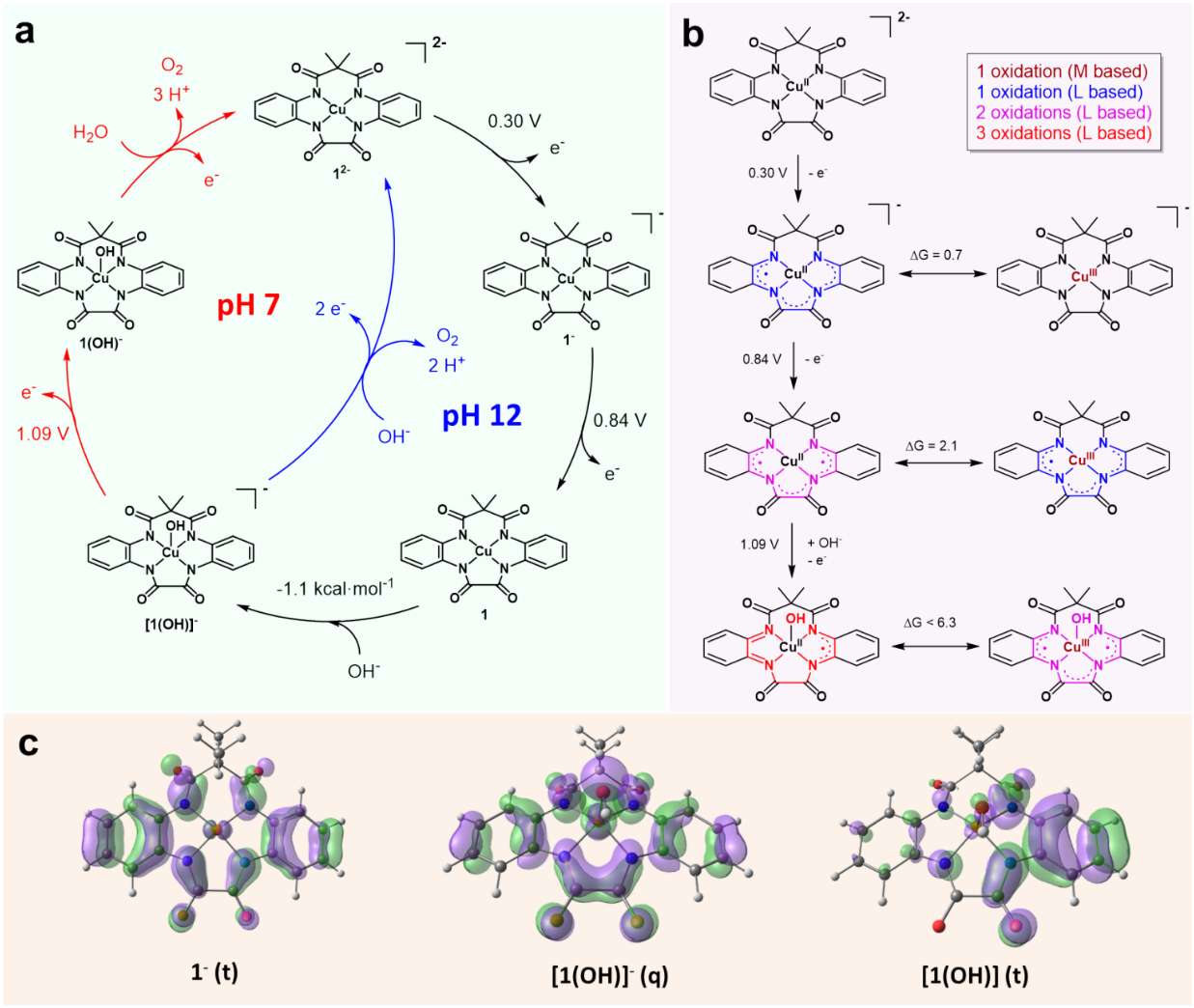

Figure 8. **a**, Schematic representation of the proposed catalytic cycle for water oxidation by complex $\mathbf{1}^{2-}$ at neutral and basic pH. The energies in the diagram are calculated free energies and the potential are the calculated values referenced to NHE. Oxidations events at 0.30 V, 0.84 V and 1.09 V leading respectively to species $\mathbf{1}^{-}$, **[1(OH)]**$^{-}$ and **[1(OH)]** are associated with the observed waves in the CV and DPV of Figure 6. **b**, Schematic representation of the electronic states corresponding to each oxidation state of complex $\mathbf{1}^{2-}$ with the calculated redox potential and the energy difference between the different multiplicities. **c**, Optimized structures and SOMO (represented in green and purple) of the intermediates relevant for the O-O bond formation. Color code for atoms: orange is copper, blue is nitrogen, red is oxygen, grey is carbon and white is hydrogen.

2.6 Stability tests and oxygen measurements.

The long-term stability of the water oxidation catalysts $\mathbf{1}^{2-}$ and $\mathbf{2}^{2-}$ were investigated based on repetitive cyclic voltammetric experiments and CPE coupled to O_2 detection analysis. The electrodes after catalysis were further analyzed based on CV, Scanning Electron Microscopy (SEM), Energy Dispersive X-ray Spectroscopy (EDX), XANES and EXAFS (Supporting Information).

Repetitive cyclic voltammetry experiments of complex $\mathbf{2}^{2-}$ shows a decrease of about 80% of the initial current density at the catalytic wave in the second cycle and thus clearly indicates the low stability against oxidative degradation of this catalyst. In sharp contrast, catalyst $\mathbf{1}^{2-}$ shows a very high oxidative stability even after 100 consecutive cycles in the -0.15 to 1.3 V range as displayed in Figure S40. Here, however, an adsorption phenomenon is observed as described in the SI (section 6), which slightly shifts the potentials of the first redox couple and decreases the catalytic current densities due to a low conductivity of the aggregate generated (Figure S20). At higher concentrations of 2 mM, this adsorption and subsequent passivation of the electrode is more drastic (Figure S38). The nature of the adsorbed layer was analyzed after catalysis by XAS showing that the local structural conformation of complex $\mathbf{1}^{2-}$ remains unchanged, as is evidenced by similar XANES spectra and K-edge energies and the same Cu-N bond distances of 1.92 Å observed both before and after catalysis by EXAFS. Importantly, no EXAFS spectral features corresponding to CuOx were observed after catalysis (Figure 3). Moreover, rinse test experiments clearly show the absence of catalytic activity of this adsorbed layer (Figures S21, S39 and S41).

A bulk electrolysis experiment coupled to O_2 detection using a Clark-type sensor was carried out and the results are presented in Figures S45-S53. In these experiments, the concentration of the catalyst was kept at the low value of 0.1 mM in order to minimize the adsorption pro-

cess. Using high surface GC plate electrode (1.0 cm^2) for a CPE experiment during 11 hours at an applied potential (E_{app}) of 1.2 V afforded 79 TONs (using the total amount of catalyst in solution) and a faradaic efficiency (FE) of 50%. The low value for the FE might be related to the oxidative degradation of the carbon electrodes. Indeed, when a similar experiment was performed in a BDD (0.5 cm^2) during 11h, 34 TONs were obtained in the same timescale with a FE close to 100% as expected for the more oxidatively robust BDD electrode. Using Savéant's formula[90,32] that takes into consideration the concentration of the electroactive catalyst within the double layer, it results in a value of approx. 6 million TONs.

Rinse tests (Figures S48 and S53) of the electrodes after the CPE discard the presence of active CuOx at the surface of the electrodes due to the lack of electroactivity. This agrees with XAS (Figure 3) and microscopy analysis (Figures S58-S65) of the same electrodes, where the spectroscopic features of copper oxide are absent. Control experiments in the absence of catalyst and using $Cu(NO_3)_2$ as the copper source confirm the catalytic activity arising from the molecular catalyst (Figures S54-S57).

3. Discussion and Conclusions

One of the key issues for the design of a molecular water oxidation catalyst is the strategy that a molecule will follow to store the four positive charges (or holes) so that they can be progressively transferred to two water molecules for their oxidation to form dioxygen.[91] The presence of redox active ancillary ligands that can be reversibly oxidized allows to have an additional site of oxidative equivalent storage and thus increases the versatility for catalyst design that in turn can lead to better control of overpotentials as well as turnover frequencies. This is particularly important for 1st row TM where the energy differences from successive oxidation states is much larger than in Ru complexes as manifested by their K-edge energies (0.8 eV per oxidation state for Ru;[92] 2.8-3.3 eV for Cr, Mn, Co;[93,94,95] and 3.1 eV for Cu (this work)). The ligand design is also important with regard to the stability of these complexes at low pH.

To take advantage of this, it is of paramount importance to understand the behavior of the redox active ligands combined with transition metals that is the interplay between the two of them when electrons are removed from the complex. For this purpose, it is useful to elucidate the main site of electron removal upon the different formal oxidation states of the complex. In this context it is interesting to see that in organic solvents the first oxidation occurs at the metal site for both $\mathbf{1}^{2-}$ and $\mathbf{2}^{2-}$ generating a diamagnetic d^8 Cu(III) ion complex. Then the second and third oxidations occur mainly at the phenyl-bisamidate units of the ligands and their redox potentials are relatively close. However, in aqueous solution it is striking to realize that for $\mathbf{2}^{2-}$ the oxidation sequence is similar as in organic solvents but for $\mathbf{1}^{2-}$ the oxidation leads to a paramagnetic species where electron density has also been removed from the π-system of the ligand.

The change in the electronic structure, or valence tautomerism, exerted by the solvent interaction evidences the energetic near degeneration in the frontier orbitals and the subsequent easy access to the different electronic states, corresponding to metal-centered, d-orbital oxidation or ligand-centered, π-orbital oxidation. This behavior determines an important redox metal-ligand cooperativity in complex $\mathbf{1}^{2-}$ upon electron removal that is absent in complex $\mathbf{2}^{2-}$, which features lower degeneration of the frontier orbitals due to the lower π-delocalization. It is impressive here how small variation on the ligands and their π-system can affect the stability of the different spin states of the complex at the different oxidation states and what is more, can have radical changes on catalyst performance.

While complex $\mathbf{2}^{2-}$ suffers decomposition during catalysis, $\mathbf{1}^{2-}$ remains stable and highly active thanks to the evidenced redox cooperativity between the metal and the ligand upon subsequent oxidations, which leads to stabilization of the accumulated oxidative equivalents by charge delocalization. Importantly, this phenomenon avoids the high energetic oxidized species centered at the ligand that can undergo oxidative degradation and high-valent metal centers that require large potentials and are frequently involved in the formation of metal oxides. The larger macrocycle size and more limited electronic π-delocalization in complex $\mathbf{2}^{2-}$ prevents such productive metal-ligand cooperation and lead to poor stability under oxidative conditions. Consistent with previous analysis, this could be attributed to the higher reactivity of the ligand-centered radical formed during oxidation that undergo fast degradation.

In addition, the stabilization against acidic demetallation and the two accessible and close ligand-based oxidations are essential characteristic of the macrocyclic ligands to enable water oxidation at neutral pH, where an extra oxidation is required to generate a more active Cu complex. In the case of catalyst $\mathbf{3}^{2-}$, which also features more limited electronic delocalization, water oxidation at pH 12 proceeds via similar initial sequence as in $\mathbf{2}^{2-}$, with a first metal oxidation and a second ligand oxidation. However, the acyclic ligand in this case, determines a more labile character of the complex, which undergoes acidic demetallation below pH 10 and prevents its application in water oxidation at neutral pH. Moreover, this complex only features one phenyl ring and thus can only accumulate one oxidative equivalent at the accessed potential. This prevents the generation of more active Cu intermediates and thus, would limit its application in water oxidation at pH 7 according to previous findings using catalyst $\mathbf{1}^{2-}$.

We envision the cooperative approach reported here for oxidative equivalent accumulation as a powerful tool for the design of more stable and efficient molecular catalyst for redox reactions. Elucidating the nature of the oxidative processes is thus essential to understand and promote productive mechanisms toward water oxidation. In this context, the frequent lack of analysis regarding irreversible precatalytic waves hinders stablishing relevant design criteria. That behavior is indicative of substantial changes in the nature of the initial molecular complexes upon oxidation, which usually leads to degradation as in the case of complex $\mathbf{2}^{2-}$. A few of the most illustrative examples of 1st row TM complexes used in water oxidation are presented in Table 1, which helps to contextualize the current achievements. As evidenced from these data, the general performances of 1st row TM

at neutral pH are limited in terms of TOF and TONs. Moreover, the scarce mechanistic information available precludes the analysis of structure-activity relationships.

In the present work we show that by using the redox active ligand strategy and properly using the molecular coordination chemistry toolkit we have managed to generate an extremely robust and fast water oxidation catalyst with a TOF_{max} of 140 s^{-1} that works even at neutral pH at very low overpotentials of 200 mV. This kinetics is also relevant compared to the fastest Ru catalysts at pH 7 when similar low overpotential values are considered via the Tafel plot, which feature TOF in the order of 10^{-2}-10.[24] In addition, we achieve an unprecedented electrochemical and spectroscopic characterization of the species involved in the catalytic cycle for 1st row TM complexes that has been supported by DFT calculations. Those studies have revealed an alternative cooperative mechanism in the accumulation of oxidative equivalents to promote water oxidation, in contrast with traditional pure metal oxidations. We expect this work will contribute to open new avenues for the design of redox non-innocent ligands for catalytic oxidations.

Table 1. Summary of the catalytic performance of different relevant complexes used for water oxidation electrocatalysis containing Cu, Fe[96], Ni[97] and Co[98]

Entry	Catalyst[h]	pH	Conditions	η (mV)	TOF_{max} (s^{-1})	TONs	Ref
1	$[(bpy)Cu(OH)_2]$	12.5	0.1 M NaOH/NaOAc	750	100[c]	0.45[a]	37
2	$[(dhbp)Cu(OH_2)_2]$	12.4	0.1 M NaOH/NaOAc	540	0.4[c]	1[a] (400)[b]	32
3	$[Cu(pyalk)_2]$	13.3	0.1 M KOH	520	0.7[c]	30[a]	40
4	$\mathbf{3}^{2-}$	11.5	0.1 M phbf[f]	700[j]	3.6[b]	0.5[a] (1.9 x10^3)[b]	31
5	$\mathbf{1}^{2-}$	7	0.1 M phbf[f]	200[j]	140[b],(162[i])	79[a] (6x10^6)[b]	tw[e]
6	$\mathbf{2}^{2-}$	7	0.1 M phbf[f]	100[j]	--	NR[g]	tw[e]
7	$[(Py_3P)Cu(OH)]^-$	8	0.1 M phbf[f]	500	20[c]	19[a]	41
8	$[Cu_2(BPMAN)(\mu\text{-}OH)]^{3+}$	7	0.1 M phbf[f]	800	0.6[c]	NR[g]	43
9	[Cu(Porf)]	7	0.1 M phbf[f]	310	30[b]	5[a]	45
10	$\{[(MeOH)Fe(HL5)]_2(\mu\text{-}O)\}^{4+}$	7	0.1 M Na_2SO_4	300	1.2[c]	NR[g]	96
11	[Ni(Porf)]	7	0.1 M phbf[f]	183	0.67[c]	NR[g]	97
12	$[Co(Py5)(OH_2)]^{2+}$	7.6	0.1 M phbf[f]	500	79[c]	NR[g]	98

[a] Calculated from bulk. [b] Calculated from Savéant's FOWA[90]. [c] Calculated from the maximum catalytic current assuming ideal S-shape response of the CV□□. [d] Mixtures of water and propylene carbonate as solvent. [e] tw stands for this work. [f] phbf is phosphate buffer. [g] NR stands for not reported. [h] ligands abbreviation used: bpy is 2,2'-bpy; dhbp is 6,6'-dihydroxy-2,2'-bpy; pyalk is 2-pyridyl-2-propanoate; Py_3P is N,N-bis(2-(2-pyridyl)ethyl)pyridine-2,6-dicarboxamidate; BPMAN is 2,7-[bis(2-pyridylmethyl)aminomethyl]-1,8-naphthyridine; Me_4Cyclam is 1,4,8,11-Tetramethyl-1,4,8,11-tetraazacyclotetradecane, Porf is tetrakis(4-*N*-methylpyridyl)porphyrin; dpaq is 2-[bis(pyridin-2-ylmethyl)]amino-*N*-quinolin-8-yl-acetamidate; HL5 (Hbbpya) is *N,N*-bis(2,2′-bipyrid-6-yl)amine; $H^{\beta F}CX\text{-}CO_2H$ is 2,3,7,8,12,13,17,18-Octafluoro-10-(4-(5-Hydroxycarbonyl-2,7-di-tert-butyl-9,9-dimethyl-xanthene))-5,15-bis(pentafluorophenyl)corrole; Py5 is 2,6-(bis(bis-2-pyridyl)methoxymethane)pyridine. [i] The value of the kinetic constant k_{obs} and thus TOF_{max} for this system has also been calculated with the approximate method assuming S-shape response of the CV. [j] The overpotential has been calculated from the DPV experiment as the potential where the maximum peak corresponding to the catalytic process appears.

ASSOCIATED CONTENT

Supporting Information.
Experimental procedures, computational details, compound characterization data, Cartesian coordinates (PDF) and X-ray data. This material is available free of charge via the Internet at http://pubs.acs.org. CIF files for complexes $\mathbf{1}^{2-}$, $\mathbf{1}^{-}$, $\mathbf{2}^{2-}$, and $\mathbf{2}^{-}$. with CCDC numbers 1959709-1959712 are available at https://www.ccdc.cam.ac.uk/

AUTHOR INFORMATION

Corresponding Author

* Antoni Llobet - Institute of Chemical Research of Catalonia (ICIQ), Barcelona Institute of Science and Technology (BIST), Tarragona, Spain, Avinguda. Països Catalans, 16,43007 Tarragona, Spain. Email: allobet@iciq.cat

Present Addresses

†Pablo Garrido-Barros - Division of Chemistry and Chemical Engineering, California Institute of Technology, Pasadena, California 91125, United States. Email: pgarrido@caltech.edu

Author Contributions

All authors have given approval to the final version of the manuscript.

Notes

The authors declare no competing financial interest.

ACKNOWLEDGMENT

Support from MINECO, FEDER and AGAUR are gratefully acknowledged (CTQ2016-80058-R, SEV-2013-0319, ENE2016-82025-REDT, CTQ2016-81923-REDC, and 2017-SGR-1631). P.G.-B acknowledges "La Caixa" Foundation for the Ph.D. grant. D.M. acknowledges support from the Severo Ochoa Excellence program (SEV-2016-0686) from the Instituto IMDEA Nanociencia and the Acciones de

Dinamización Europa Investigacion grant (EIN2019-103399). XAS experiments were performed at the CLAESS beamline at ALBA Synchrotron with the beamline support of the ALBA staff under proposal No. 2016091818, and additionally used resources of sector 20 beamline at the Advanced Photon Source (APS) at Argonne National Laboratory. Sector 20 beamline at APS is operated by the U.S DOE and the Canadian Light Source.

REFERENCES

[1] Steffen, W.; Rockström, J.; Richardson, K.; Lenton, T. M.; Folke, C.; Liverman, D.; Summerhayes, C. P.; Barnosky, A. D.; Cornell, S. E.; Crucifix, M.; Donges, J. F.; Fetzer, I.; Lade, S. J.; Scheffer, M.; Winkelmann, R.; Schellnhuber, H. J. Trajectories of the Earth System in the anthropocene. *Proc. Natl Acad. Sci. USA* **2018**, *115*, 8252–8259.

[2] Balmaseda, M. A.; Trenberth, K. E.; Källén, W. Distinctive climate signals in reanalysis of global ocean heat content. *Geophys. Res. Lett.* **2013**, *40*, 1754–1759.

[3] The Intergovernmental Panel on Climate Change (IPCC). *Climate Change 2014: Mitigation of Climate Change* (eds Edenhofer, O. et al.) (Cambridge Univ. Press, 2014).

[4] United Nations. *Adoption of the Paris Agreement: Proposal by the President*. UNFCCC https://unfccc.int/resource/docs/2015/cop21/eng/l09.pdf (2015).

[5] Staher, W. R. The circular economy. *Nature* **2016**, *531*, 435–438.

[6] Grätzel, M. Artificial photosynthesis: water cleavage into hydrogen and oxygen by visible light. *Acc. Chem. Res.* **1981**, *14*, 376–384.

[7] Lewis, N. S. Research opportunities to advance solar energy utilization. *Science* **2016**, *351*, 353–361.

[8] Nocera, D. G. Solar fuels and solar chemicals industry. *Acc. Chem. Res.* **2017**, *50*, 616–619.

[9] Melis, A. Photosynthesis-to-fuels: from sunlight to hydrogen, isoprene, and botryococcene production. *Energy Environ. Sci.* **2012**, *5*, 5531–5539.

[10] Garrido-Barros, P.; Funes-Ardoiz, I.; Farrás, P.; Gimbert-Suriñach, C.; Maseras, F.; Llobet, A. in *Science of Synthesis: Catalytic Oxidations in Organic Synthesis*. (ed. Muniz, K.) (Georg Thieme Verlag, 2018).

[11] McEvoy, J. P.; Brudvig, G. W. Water-splitting chemistry of photosystem II. *Chem. Rev.* **2006**, *106*, 4455–4483.

[12] Cox, N., Pantazis, D. A.; Neese, F.; Lubitz, W. Biological water oxidation. *Acc. Chem. Res.* **2013**, *46*, 1588–1596.

[13] Nelson, N.; Ben-She, A. The complex architecture of oxygenic photosynthesis. *Nat. Rev. Mol. Cell Biol.* **2004**, *5*, 971–982.

[14] Berardi, S.; Drouet, S., Francás, L.; Gimbert-Suriñach, C.; Guttentag, M.; Richmond, C.; Stoll, T.; Llobet, A. Molecular artificial photosynthesis. *Chem. Soc. Rev.* **2014**, *43*, 7501–7519.

[15] Godwin, I.; Rovetta, A.; Lyons, M.; Coleman, J. Electrochemical water oxidation: the next five years. *Curr. Opin. Electrochem.* **2018**, *7*, 31–35.

[16] Blakemore, J. D.; Crabtree, R. H.; Brudvig, G. W. Molecular catalysts for water oxidation. *Chem. Rev.* **2015**, *115*, 12974-13005.

[17] McCrory, C. C. L.; Jung, S.; Ferrer, I. M.; Chatman, S. M.; Peters, J. C.; Jaramillo, T. F. Benchmarking hydrogen evolving reaction and oxygen evolving reaction electrocatalysts for solar water splitting devices. *J. Am. Chem. Soc.* **2015**, *137*, 4347–4357.

[18] Garrido-Barros, P.; Gimbert-Suriñach, C.; Matheu, R.; Sala, X.; Llobet, A. How to make an efficient and robust molecular catalyst for water oxidation. *Chem. Soc. Rev.* **2017**, *46*, 6088–6098.

[19] Matheu, R.; Garrido-Barros, P.; Gil-Sepulcre, M.; Ertem, M. Z.; Sala, X.; Gimbert-Suriñach, C.; Llobet, A. The development of molecular water oxidation catalysts. *Nat. Rev. Chem.* **2019**, *3*, 331-341.

[20] Garrido-Barros, P.; GimbertSuriñach, C.; Moonsiram, D.; Picón, A.; Monge, P.; Batista, V. S.; Llobet, A. Electronic π-delocalization boots catalytic water oxidation by Cu(II) molecular catalysts heterogenized on graphene sheets. *J. Am. Chem. Soc.* **2017**, *139*, 12907-12910.

[21] Alibabaei, L.; Sherman, B. D.; Norris, M. R.; Brennaman, M. K.; Meyer, T. J. Visible photoelectrochemical water splitting into H2 and O2 in a dye-sensitized photoelectrosynthesis cell. *Proc. Natl. Acad. Sci. U. S. A.* **2015**, *112*, 5899–5902.

[22] Matheu, R.; Moreno-Hernandez, I. A.; Sala, X.; Gray, H. B.; Brunschwig, B. S.; Llobet, A.; Lewis, N. S. Photoelectrochemical behavior of a molecular Ru-based water-oxidation catalyst bound to TiO_2-protected Si photoanodes. *J. Am. Chem. Soc.* **2017**, *139*, 11345–11348.

[23] Ezhov, R.; Ravari, A. K.; Page, A.; Pushkar, Y. Water oxidation catalyst cis- [Ru(bpy)(5,5′-dcbpy)(H2O)2]2+ and Its Stabilization in Metal–Organic Framework. *ACS Catal.* **2020**, *10*, 5299-5308.

[24] Matheu, R.; Ertem, M. Z.; Gimbert-Suriñach, C.; Sala, X.; Llobet, A. Seven coordinated molecular ruthenium-water oxidation catalysts: A coordination chemistry journey. *Chem. Rev.* **2019**, *119*, 3453-3471.

[25] Roger, I.; Shipman, M.; Symes, M. Earth-abundant catalysts for electrochemical and photoelectrochemical water splitting. *Nat. Rev. Chem.* **2017**, *1*, 0003.

[26] Kärkäs, M. D.; Åkermark, B. Water oxidation using earth-abundant transition metal catalysts: opportunities and challenges. *Dalton Trans.* **2016**, *45*, 14421-14461.

[27] Ezhov, R.; Ravari, A. K.; Pushkar, Y. Characterization of the Fe^{V}=O complex in the pathway of water oxidation. *Angew. Chem.* **2020**, DOI: 10.1002/ange.202003278.

[28] Storr, T.; Verma, P.; Pratt, R. C.; Wasinger, E. C.; Shimazaki, Y.; Stack, T. D. P. Defining the electronic and geometric structure of one-electron oxidized copper-bis-phenoxide complexes. *J. Am. Chem. Soc.* **2008**, *130*, 15448–15459.

[29] Gary, J. G.; Citek, C.; Brown, T. A.; Zare, R. N.; Wasinger, E. C.; Stack, T. D. P. Direct copper(III) formation from O_2 and copper(I) with histamine ligation. *J. Am. Chem. Soc.* **2016**, *138*, 9986–9995.

[30] Anson, F. C.; Collins, T. J.; Richmond, T. G.; Santarsiero, B. D.; Toth, J. E.; Treco, B. G. T. Highly stabilized copper(III) complexes. *J. Am. Chem. Soc.* **1987**, *109*, 2979-2991.

[31] Garrido-Barros, P.; Funes-Ardoiz, I.; Drouet, S.; Benet-Buchholz, J.; Maseras, F.; Llobet, A. Redox non-innocent ligand controls water oxidation overpotential in a new family of mononuclear Cu-based efficient catalysts. *J. Am. Chem. Soc.* **2015**, *137*, 6758–6761.

[32] Zhang, T.; Wang, C.; Liu, S.; Wang, J.-L.; Lin, W. A Biomimetic Copper Water Oxidation Catalyst with Low Overpotential. *J. Am. Chem. Soc.* **2014**, *136*, 273-281.

[33] Muckerman, J. T.; Polyansky, D. E.; Wada, T.; Tanaka, K.; Fujita, E. Water oxidation by a ruthenium complex with noninnocent quinone ligands: possible formation of an O-O bond at a low oxidation state of the metal. *Inorg. Chem.* **2008**, *47*, 1787-1802.

[34] Boyer, J. L.; Rochford, J.; Tsai, M.-K.; Muckerman, J. T.; Fujita, E. Ruthenium complexes with non-innocent ligands: Electron distribution and implications for catalysis. *Coord. Chem. Rev.* **2010**, *254*,

309-330.

[35] Shi, J.; Guo, Y.-H.; Xie, F.; Chen Q.-F.; Zhang, M. T. Redox-active ligand assisted catalytic water oxidation by Ru(IV)=O intermediate. *Angew. Chem., Int. Ed.* **2020**, *59*, 2-11.

[36] Ravari, A. K.; Zhu, G.; Ezhov, R.; Pineda-Galvan, Y.; Page, A.; Weinschenk, W.; Yan, L.; Pushkar, Y. Unraveling the mechanism of catalytic water oxidation via *de novo* synthesis of reactive intermediate. *J. Am. Chem. Soc.* **2020**, *142*, 884-893.

[37] Barnett, S. M.; Goldberg, K. I.; Mayer, J. M. A soluble copper–bipyridine water-oxidation electrocatalyst. *Nat. Chem.* **2012**, *4*, 498–502.

[38] Zhang, M.-T.; Chen, Z. F.; Kang, P.; Meyer, T. J. Electrocatalytic water oxidation with a copper(II) polypeptide complex. *J. Am. Chem. Soc.* **2013**, *135*, 2048–2051.

[39] Gerlach, D. L.; Bhagan, S.; Cruce, A. A.; Burks, D. B.; Nieto, I.; Truong, H. T.; Kelley, S. P.; Herbst-Gervasoni, C. J.; Jernigan, K. L.; Bowman, M. K.; Pan, S.; Zeller, M.; Papish, E. T. Studies of the pathways open to copper water oxidation catalysts containing proximal hydroxy groups during basic electrocatalysis. *Inorg. Chem.* **2014**, *53*, 12689–12698.

[40] Fisher, K. J.; Materna, K. L.; Mercado, B. Q.; Crabtree, R. H.; Brudvig, G. W. Electrocatalytic water oxidation by a copper(II) complex of an oxidation-resistant ligand. *ACS Catal.* **2017**, *7*, 3384–3387.

[41] Coggins, M. K.; Zhang, M.-T.; Chen, Z. F.; Song, N.; Meyer, T. J. Single-site copper(II) water oxidation electrocatalysis: rate enhancements with HPO_4^{2-} as a proton acceptor at pH 8. *Angew. Chem., Int. Ed.* **2014**, *53*, 12226–12230.

[42] Chen, F.; Wang, N.; Lei, H.; Guo, D.; Liu, H.; Zhang, Z.; Zhang, Z.; Lai, W.; Cao, R. Electrocatalytic water oxidation by a water-soluble copper(II) complex with a copper-bound carbonate group acting as a potential proton shuttle. *Inorg. Chem.* **2017**, *56*, 13368-13375.

[43] Su, X.-J.; Gao, M.; Jiao, L.; Liao, R.-Z.; Siegbahn, P. E. M.; Cheng, J.-P.; Zhang, M.-T. Electrocatalytic water oxidation by a dinuclear copper complex in a neutral aqueous solution. *Angew. Chem., Int. Ed.* **2015**, *54*, 4909–4914.

[44] Prevedello, A.; Bazzan, I.; Carbonare, N. D.; Giuliani, A.; Bhardwaj, S.; Africh, C.; Cepek, C.; Argazzi, R.; Bonchio, M.; Caramori, S.; Robert, M.; Sartorel, A. Heterogeneous and homogeneous routes in water oxidation catalysis starting from Cu^{II} complexes with tetraaza macrocyclic ligands. *Chem.–Asian J.* **2016**, *11*, 1281-1287.

[45] Liu, Y.; Han, Y.; Zhang, Z.; Zhang, W.; Lai, W.; Wang, Y.; Cao, R. Low overpotential water oxidation at neutral pH catalyzed by a copper(II) porphyrin. *Chem. Sci.* **2019**, *10*, 2613-2622.

[46] Chen, Z.; Meyer T. J. Copper(II) catalysis of water oxidation. *Angew. Chem. Int. Ed.* **2013**, *52*,700-703.

[47] Yu, F.; Lei, F.; Zhang, B.; Li, H.; Sun, L. Efficient Electrocatalytic Water Oxidation by a Copper Oxide Thin Film in Borate Buffer. *ACS Catal.* **2015**, *5*, 627-630.

[48] Liu, X.; Jia, H.; Sun, Z.; Chen, H.; Xu, P.; Du. P. Nanostructured copper oxide electrodeposited from copper(II) complexes as an active catalyst for electrocatalytic oxygen evolution reaction. *Electrochem. Commun.* **2014**, *46*, 1-4.

[49] Li, T.-T.; Cao, S.; Yang, C.; Chen, Y.; Lv, X.-J.; Fu, W.-F. Electrochemical Water Oxidation by In Situ-Generated Copper Oxide Film from $[Cu(TEOA)(H_2O)_2][SO_4]$ Complex. *Inorg. Chem*. **2015**, *54*, 3061-3067.

[50] Cabbiness, D. K.; Margerum, D. W. Macrocyclic effect on the stability of copper(II) tetramine complexes. *J. Am. Chem. Soc.* **1969**, 91, 6540-6541.

[51] Cabbiness, D. K.; Margerum, D. W. Effect of macrocyclic structures on the rate of formation and dissociation of copper(II) complexes. *J. Am. Chem. Soc.* **1970**, *92*, 2151-2153.

[52] Hancock, R. D.; McDougall, G. J. Origin of Macrocyclic Enthalpy. *J. Am. Chem. Soc.* **1980**, *102*, 6553-6555.

[53] Kodama, M ; Kimura, E. The 13-membered macrocyclic effect. Polarographic studies of copper(II)-1,4,7,10-tetraazacyclotridecane complexation. *J. Chem. Soc., Chem. Commun.* **1975**, 891-892.

[54] Lam, B. M. T.; Halfen J. A.; Young, C. G.; Hagadorn, J. R.; Holland, P. L.; Lledós, A.; Cucurull-Sánchez, L.; Novoa, J. J.; Alvarez, S.; To,man, W. B. Ligand Macrocycle structural effects on copper-dioxygen reactivity. *Inorg. Chem.* **2000**, *18*, 4059-4072.

[55] Lindoy, L. F. The chemistry of macrocyclic ligand complexes (Cambridge University Press, 2009)

[56] Ellis, W. C.; McDaniel, N. D.; Bernhard, S.; Collins, T. J. Fast water oxidation using iron. *J. Am. Chem. Soc.* **2010**, *132*, 10990-10991.

[57] Van Leest, N. P.; Tepaske, M. A.; Oudsen, J.-P. H.; Venderbosch, B.; Rietdijk, N. R.; Siegler, M. A.; Tromp, M.; van der Vlugt, J. I.; de Bruin, B. Ligand redox noninnocence in $[Co^{III}(TAML)^{0/-}$ complexes affects nitrene formation. *J. Am. Chem. Soc.* **2020**, *142*, 552-563.

[58] Du, H.-Y.; Chen, S.-C.; Su, X.-J.; Jiao, L.; Zhang, M.-T. Redox-active ligand assisted multielectron catalysis: a case of Co^{III} complex as water oxidation catalyst. *J. Am. Chem. Soc.* **2018**, *140*, 1557-1565.

[59] Panda, C.; Debgupta, J.; Díaz, D. D.; Singh, K. K.; Gupta, S. S.; Dhar, B. B. Homogeneous photochemical water oxidation by biuret-modified Fe-TAML: evidence of $Fe^{V}(O)$ intermediate. *J. Am. Chem. Soc.* **2014**, 136, 12273-12282.

[60] Das, D.; Pattanayak, S.; Singh, K. K.; Garai, B.; Gupta, S. S. Electrocatalytic water oxidation by a molecular cobalt complex through a high valent cobalt oxo intermediate. *Chem. Commun.* **2016**, *52*, 11787-11790.

[61] Ertem, M. Z.; Gagliardi, L.; Cramer, C. J. Quantum chemical characterization of the mechanism of an iron-based water oxidation catalyst. *Chem. Sci.* **2012**, *3*, 1293-1299.

[62] Liao, R.-Z.; Li, X.-C.; Siegbahn, P. E. M. Reaction mechanism of water oxidation catalyzed by Iron tetraamido macrocyclic ligand complexes-a DFT study. *Eur. J. Inorg. Chem.* **2014**, 728-741.

[63] Lee, H.; Wu, X.; Sun, L. Homogeneous electrochemical wa-ter oxidation at neutral pH by water-soluble NiII complexes bearing redox non-innocent tetraamido macrocyclic ligands. ChemSusChem 2020, 13, 3277-3282.

[64] Ellis, W. C.; Tran, C. T.; Roy, R.; Rusten, M.; Fischer, A.; Ryabov, A. D.; Blumberg, B.; Collins, T. J. Designing Green Oxidation Catalysts for Purifying Environmental Waters. *J. Am. Chem. Soc.* **2010**, *132*, 9774-9781.

[65] Kojima, T.; Ogishima, F.; Nishibu, T.; Kotani, H.; Ishizuka, T.; Okajima, T.; Nozawa, S.; Shiota, Y.; Yoshizawa, k.; Ohtsu, H.; Kawano, M.; Shiga, T.; Oshio, H. Intermediate-spin Iron(III) complexes having a redox-noninnocent macrocyclic tetraamido ligand. *Inorg. Chem.* **2018**, *57*, 9683-9695.

[66] Abdulmalic, M. A.; Aliabadi, A.; Petr, A.; Krupskaya, Y.; Kataev, V.; Büchner, B.; Zaripov, R.; Vavilova E.; Voronkoca, V.; Salikov, K.; Hahn, T.; Kortus, J.; Meva, F. E.; Schaarschmidt, D.; Rüffer, T. Magnetic superexchange interactions: trinuclear bis(oxamidate) versus bis(oxamato) type complexes. *Dalton Trans*. **2015**, *44*, 8062–8079.

[67] Zahran, Z. N.; Tsubonouchi, Y.; Mohamed, E. A.; Yagi, M. Recent advances in the development of molecular Catalyst-based

anodes for water oxidation toward artificial photosynthesis. *ChemSusChem.* **2019**, *12*, 1775-1793.

[68] Garrido-Barros, P.; Matheu, R.; Gimbert-Suriñach, C.; Llobet, A. Electronic, mechanistic and structural factors that influence the performance of molecular water oxidation catalysts anchored on electrode surfaces. *Current Opinion in Electrochemistry* **2019**, *15*, 140-147.

[69] Baker, M. L.; Mara, M. W.; Yan, J. J.; Hodgson, K. O.; Hedman, B.; Solomon, E. I. K- and L-edge X-ray absorption spectroscopy (XAS) and resonant inelastic X-ray scattering (RIXS) determination of differential orbital covalency (DOC) of transition metal sites. *Coord. Chem. Rev.* **2017**, *345*, 182-208.

[70] Smith, T. A.; Penner-Hahn, J. E.; Berding, M. A.; Doniach, S.; Hodgson, K. O. Polarized x-ray absorption edge spectroscopy of single-crystal copper(II) complexes. *J. Am. Chem. Soc.* **1985**, *107*, 5945-5955.

[71] Thomson, N. C.; Wiliams, K. D.; Dai, X.; Sproules, S.; DeBeer, S.; Warren, T. H.; Wieghardt, K. Re-evaluating the Cu K pre-edge XAS transition in complexes with covalent metal-ligand interactions. *Chem. Sci.* **2015**, *6*, 2474-2487.

[72] Gaur, A.; Klysubun, W.; Joshi, S. K.; Soni, B.; Shrivastava, B. D.; Prasadm J.; Srivastava, K. XAFS study of copper(II) diethylenetriamine complexes having different coordination geometries. *Journal of Physics: Conference Series,* **2016**, *712*, 012084.

[73] DeBeer, S.; Randall, D. W.; Nersissian, A. M.; Valentine, J. S.; Hedman, B.; Hodgson, K. O.; Solomon, E. I. X-ray absorption Edge and EXAFS studies of 89the Blue Copper Site in Stellacyanin: Effects of Axial Amide Coordination. *J. Phys. Chem. B.* **2000**, *104*, 10814-10819.

[74] Hunt, C., Peterson, M.; Anderson, C.; Chang, T.; Wu, G.; Scheiner, S.; Ménard, G. Switchable aromaticity in an isostructural Mn phthalocyanine series isolated in five separate redox states. *J. Am. Chem. Soc.* **2019**, ***141***, 2604-2613.

[□□] Ruiz, R.; Surville-Barland, C.; Aukauloo, A.; Anxolabehere-Mallart, E.; Journaux, Y.; Cano, J.; Muñoz, M. C. Stabilization of copper(III) complexes by disubstituted oxamides and related ligands. *J. Chem. Soc., Dalton Trans.,* **1997**, 745-751.

[76] Solomon, E. I.; Heppner, D. E.; Johnston, E. M.; Ginsbach, J. W.; Cirera, J.; Qayyum, M.; Kieber-Emmons, M. T.; Kjaergaard, C. H.; Hadt, R. G.; Tian, L. Copper active sites in biology. *Chem. Rev.* **2014**, *114*, 3659-3853.

[77] DuBois, J. L.; Mukherjee, P.; Stack, T. D. P.; Hedman, B.; Solomon, E. I.; Hodgson, K. O. A systematic K-edge X-ray absorption spectroscopic study of Cu(III) sites. *J. Am. Chem. Soc.* **2000**, *122*, 5775-5787.

[78] DuBois, J. L.; Mukherjee, P.; Collier, A. M.; Mayer, J. M.; Solomon, E. I.; Hedman, B.; Stack, T. D. P., Hodgson, K. O. Cu K-edge XAS study of the $[Cu_2(\mu\text{-}O)_2]$ core: direct experimental evidence for the presence of Cu(III). *J. Am. Chem. Soc.* **1997**, *119*, 8578-8579.

[79] Anson, F. C.; Collins, T. J.; Richmond, T. G.; Santrsiero, B. D.; Toth, J. E.; Treco, B. G. R. T. Highly stabilized copper(III) complexes. *J. Am. Chem. Soc.* **1987**, *109*, 2974-2979

[□□] Wang, Y.; Stack, T. D. P. Galactose oxidase model complexes: catalytic reactivities. *J. Am. Chem. Soc.* **1996**, *118*, 13097-13098.

[□1] Verma, P.; Pratt, R.; Storr, T.; Wasinger, E. C.; Stack, T. D. P. Sulfanyl stabilization of copper-bonded phenoxyls in model complexes and galactose oxidase. *Proc. Natl. Acad. Scie USA* **2011**, *108*, 18600-18605.

[□2] Osorio, M.; Jarjayes, O.; Kanso, H.; Philouze, C.; Neese, F.; Thomas, F.; X-Ray structures of copper(II) and nickel(II) radical salen complexs: the preference of galactose oxidase for copper(II). *Angew. Chem. Int. Ed.* **2010**, *49*, 4989-4992.

[83] Demir, S.; Jeon, I.-R.; Long, J. R.; Harris, T. D. Radical ligand-containing single-molecule magnets. *Coord. Chem. Rev.* **2015**, *289-290*, 149-176.

[84] Peeks, M. D.; Tait, C. E.; Neuhaus, P.; Fischer, G. M.; Hoffmann, M.; Haver, R.; Cnossen, A.; Harmer, J. R.; Timmel, C. R.; Anderson, H. L. Electronic delocalization in the radical cations of porphyrin oligomer molecular wires *J. Am. Chem. Soc.* **2017**, *139*, 10461-10471.

[85] Richert, S.; Tait, C. E.; Timmel,C. R. Delocalisation of photoexcited triplet states probed by transient EPR and hyperfine spectroscopy *J. Magn. Reson.* **2017**, *280*, 103-116.

[86] Chłopek, K.; Bothe, E.; Neese, F.; Weyhermüller, T.; Wieghardt, K. *Inorg. Chem.* **2006**, *45*, 6298-6307.

[87] Naqvi, K. R.; Melø, T. B. Reduction of tetranitromethane by electronically excited aromatics in acetonitrile: Spectra and molar absorption coefficients of radical cations of anthracene, phenanthrene and pyrene. *Chem. Phys. Lett*. **2006**, *428*, 83–87.

[88] Matheu, R.; Neudeck, S.; Meyer, F.; Sala, C.; Llobet, A. Foot of the wave analysis for mechanistic elucidation and benchmarking applications in molecular water oxidation catalysis. *ChemSusChem* **2016**, *9*, 3361-3369.

[□□] Funes-Ardoiz, I.; Garrido-Barros, P.; Llobet, A.; Maseras, F. Single electron transfer steps in water oxidation catalysis: redefining the mechanistic scenario. *ACS Catal.* **2017**, *7*, 1712-1719

[90] Costentin, C.; Drouet, S.; Robert, M.; Savéant, J.-M. Turnover Numbers, Turnover Frequencies, and Overpotential in Molecular Catalysis of Electrochemical Reactions. Cyclic Voltammetry and Preparative-Scale Electrolysis. *J. Am. Chem. Soc.* **2012**, *134*, 11235-11242.

[91] Romain, S.; Vigara, L.; Llobet, A. Oxygen-oxygen bond formation pathways promoted by Ruthenium complexes. *Acc. Chem. Res.* **2009**, 42, 1944-1953.

[92] Planas, N.; Vigara, L.; Cady, C.; Miró, P.; Huang, P.; Hammarström, L.; Styring, S.; Leider, N.; Dau, H.; Haumann, M.; Gagliardi, L.; Cramer, C. J.; Llobet, A. Electronic Structure of Oxidized Complexes Derived from cis-$[Ru^{II}(bpy)_2(H_2O)_2]^{2+}$ and its Photoisomerization Mechanism. *Inorg. Chem*. **2011**, *50*, 11134-11142.

[93] Schrapers, P.; Mebs, S.; Goetzl, S.; Hennig, S. E.; Dau, H.; Dobbek, H.; Haumann, M. Axial Ligation and Redox Changes at the Cobalt Ion in Cobalamin Bound to Corrinoid Iron-Sulfur Protein (CoFeSP) or in Solution Characterized by XAS and DFT. PLoS ONE 11(7): e0158681. https://doi.org/10.1371/journal.pone.0158681 (2016).

[94] Karel, J.; Bernardi, F.; Wang, C.; Stinshoff, R.; Born, N.-O.; Ouardi, S.; Burkhardt, U.; Fecher, G. H.; Felser, C. Evidence for localized moment picture in Mn-based Heusler compounds. *Phys. Chem. Chem. Phys*. **2015**, *17*, 31707-31714.

[95] Arčon, I.; Mirtič, B.; Kodre, A. Determination of valence states of chromium in calcium chromates by using X-ray Absorption Near-Edge Structure (XANES) Spectroscopy. J. Am. Ceram. Soc. 1998, 81, 222-224.

[96] Kottrup, K. G.; D'Agostini, S.; van Langevelde, P. H.; Siegler, M. A.; Hetterscheid, D. G. Catalytic activity of an iron-based water oxidation catalyst: substrate effects of graphitic electrodes. *ACS Catal.* **2018**, *8*, 1052-1061.

[97] Han, Y.; Wu, Y.; Lai, W.; Cao, R. Electrocatalytic Water oxidation by a water-soluble nickel porphyrin complex at neutral pH with low overpotential. *Inorg. Chem*. **2015**, *54*, 5604−5613.

[98] Wasylenko, D. J.; Ganesamoorthy, C.; Borau-Garcia, J.; Berlinguette, C. P. Electrochemical evidence for catalytic water oxida-

tion mediated by a high-valent cobalt complex. *Chem. Commun.* **2011**, *47*, 4249-4251.

[99] Costentin, C.; Savéant, J.-M. Multielectron, Multistep Molecular Catalysis of Electrochemical Reactions: Benchmarking of Homogeneous Catalysts. *ChemElectroChem* **2014**, *1*, 1226-1236.

Insert Table of Contents artwork here